ACSNANO

www.acsnano.org

ARTICLE

Magnetic Soft Robot for Minimally Invasive Urethral Catheter Biofilm Eradication

Polina I. Baburova, Daniil V. Kladko, Alina Lokteva, Anna Pozhitkova, Viktoriya Rumyantceva, Valeriya Rumyantceva, Ilya V. Pankov, Sergey Taskaev, and Vladimir V. Vinogradov*

Cite This: *ACS Nano* 2023, 17, 20925−20938

Read Online

ACCESS | Metrics & More | Article Recommendations | Supporting Information

ABSTRACT: **Catheter-related biofilm infection remains the main problem for millions of people annually, affecting morbidity, mortality, and quality of life. Despite the recent advances in the prevention of biofilm formation, alternative methods for biofilm prevention or eradication still should be found to avoid traumatic and expensive removal or catheter replacement. Soft magnetic robots have drawn significant interest in favor of remote control, fast response, and wide space for design. In this work, we demonstrated magnetic soft robots as a minimally invasive, safe, and effective approach to eliminate biofilm from urethral catheters (20 Fr or 5.1 mm in diameter). Seven designs of the robot were fabricated (size 4.5 × 15 mm), characterized, and tested in the presence of a rotating magnetic field. As a proof-of-concept, we demonstrated the superior efficiency of biofilm removal on the model of a urethral catheter using a magnetic robot, reaching full eradication for the octagram-shaped robot (velocity 2.88 ± 0.6 mm/s) at a 15 Hz frequency and a 10 mT amplitude. These findings are helpful for the treatment of biofilm-associated catheter contamination, which allows an increase in the catheter wearing time without frequent replacement and treatment of catheter-associated infections.**

KEYWORDS: *soft robot, elastomer, magnetic actuation, biofilm removal, urethral catheters*

INTRODUCTION

The biofilm-associated infection on the invasive device during surgical or medical treatment has a tremendous impact on healthcare. Seventy percent of healthcare-associated infections (HAIs) are connected with medical device insertion,[1] involving over 600 million people worldwide annually. Most of them suffer from catheter-associated urinary tract infection (CAUTI), catheter-related bloodstream infections (CRBSI), and ventilator-associated pneumonia (VAP).[2−4] The HAI problem is a grave issue for healthcare and patients, affecting hospital stay, morbidity, and mortality, especially for people over the age of 65.[5] For example, in 2011 the HAIs in Europe caused 16 million extra days of stay in hospitals, which led to ∼7 billion euros in additional costs.[5] Accordingly, in epidemiology studies, urinary tract infections, the most frequent cause of HAIs and CAUTIs alone, cause more than 13 000 deaths every year in the USA alone.[6,7] The most common microorganisms associated with biofilm formation on urinary and central venous catheters are *Escherichia coli*, *Pseudomonas aeruginosa*, *Candida* spp., *Enterococcus* spp., *Klebsiella* spp., *Proteus* spp., *Streptococcus* spp., *Enterobacter* spp., *Citrobacter* spp., and *Staphylococcus aureus*.[8,9]

The common approaches to preventing catheter-associated infection include the development of an antifouling surface,[10−12] antimicrobial catheter coatings,[13,14] contact killing approaches,[15] and frequent catheter replacement.[9,16] The antifouling surface focuses on the prevention of biofilm formation through an antiadhesive surface based on hydrophilic and zwitterionic polymers.[17−19] However, such a catheter works as an electrostatic or wetting barrier for adhering, without biological activity against bacteria, which leads to only a delay of biofilm formation and is unsuitable for long-term catheterization.[8,20] Another strategy is a wide range of antimicrobial coatings or release agents based on antibiotics, enzymes, quorum sensing inhibition, antiseptics, metal ions, or nanoparticles.[21−25] The drawbacks of such methods arise from the

Received: October 11, 2022
Revised: October 14, 2023
Accepted: October 18, 2023
Published: October 23, 2023

increase of antibiotic resistance in the world,[26] enzyme stability issues,[27] possible pathogenicity appearing for quorum sensing inhibitors,[28] and toxicity and selectivity issues for antiseptics and metal ions or nanoparticles. Therefore, there is no efficient method for early biofilm prevention or eradication besides the traumatic and costly removal or replacement of contaminated devices.

There is a strong need for an alternative methodology to address catheter-associated infections, which could be found in mechanical-force-based concepts to eliminate biofilm. In addition to passive bacteria killing via bactericidal cicada-like surfaces and particles,[29−31] magnetically controlled micro- and nanoparticles have garnered much attention.[32] Generally, a magnetic field is a noninvasive and biologically safe approach that provides an interesting opportunity to bring thermal or mechanical stimuli through a magnetic particle.[33] Such implementation of a magnetic force-based approach can be found in the fields of minimally invasive surgery,[34,35] soft robotics,[36,37] disease treatment,[38−40] and remote behavior control. Examples of biofilm eradication include magnetic microswarms for target elimination of biofilm occlusion,[41] catalytic antimicrobial nanorobots and millirobots that can be delivered through narrow and hard-to-reach areas,[42,43] and pollen-grain-based microswarms for biliary stent biofilm eradication.[43] The work of such a swarm dynamic system is based on an alternating or rotating magnetic field, which drives the microrobot and provides sufficient mechanical forces to the biofilm. The possible drawbacks of nano- and microrobot-based approaches are the toxicity issue, difficulties with precise navigation in a viscous media in human-scale vessels, and low mechanical force for mature and tough biofilm eradication. Alternatively, untethered magnetic soft robots could easily navigate and perform a site-specific task inside hard-to-reach sites under the action of a magnetic field, even on the human body scale.[44] These materials consist of soft matrices with embedded hard magnetic particles, and the interaction between the magnetic torque and internal mechanical force allows for the remote control of such systems. The mechanical force from such magnetic soft robots has already shown their effectiveness for model thrombosis treatment,[45,46] drug or object delivery,[47,48] and catheter guiding for surgical applications.[35,49]

Herein, we demonstrate the use of magnetic soft robots for biofilm eradication in vitro. We described the robot evolution design, starting from the simple 2D plate to the 3D octagram, to find the most efficient robot for biofilm elimination. Seven robot designs were fabricated, characterized, and tested in the presence of a rotating magnetic field (5−30 Hz frequency and 1−15 mT amplitude) with an analysis of the robot's rotational frequency and forward speed. Further, we demonstrated the full biofilm removal on the model of a 20 Fr urethral catheter for Gram-positive and Gram-negative bacteria (*Pseudomonas aeruginosa* and *Staphylococcus aureus*) strains by magnetic soft robots under the action of a rotating magnetic field (at 15 Hz frequency and 10 mT amplitude).

RESULTS AND DISCUSSION

Catheters represent one of the most frequently used medical equipment in practice.[10] Fairly often, catheter usage causes different infections, related to central venous catheterization, urethral tract catheterization, gastrostomy, and endotracheal intubation. In this work, we focus on the infection of indwelling urethral catheters as the most widespread cause of HAIs (Figure 1A). These catheters are built from rubber, plastic (PVC), or silicone with an average size of 14−16 Fr for men and 10−12 Fr for women (1 Fr = 0.33 mm).[50] The unification of the catheter materials and their sizes gives hope for a possible solution for the translation of the biofilm-associated problem from one type of catheter to another.

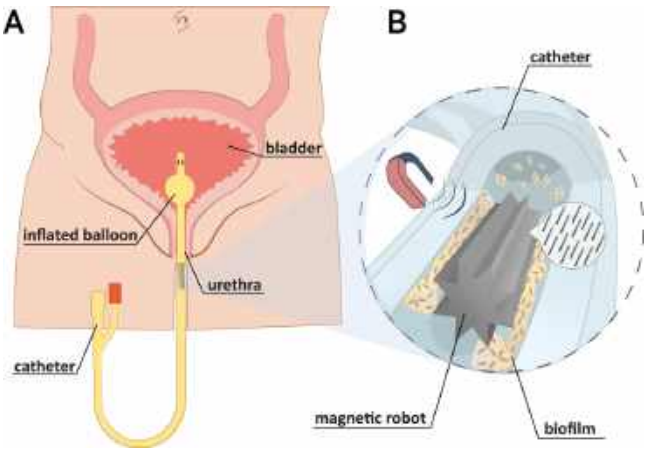

Figure 1. Schematic illustration of magnetic soft robot for biofilm removal. Illustration of the proposed concept of cleaning biofilm from a urethral catheter with a soft robot, actuated by a magnetic field. (A) Urethral catheter wearing; (B) proposed magnetic soft robot for biofilm removal.

Despite the trivial increase in inflammation probability, the frequent replacement of catheters also affects quality of life, painful and stressful procedures, and the number of nonreusable silicone catheters. The untethered magnetic soft robot with a specific design could potentially clean the biofilm from the catheter surface during long-term wear by shear stress-based fluid mechanical forces. The magnetic robot could be driven by a rotating magnetic field and provide sufficient magneto-mechanical coupling to ensure entire biofilm cleaning (Figure 1B). Such treatment could increase the catheter's wearing time without frequent replacement.

Our proposed robot consists of an elastomer matrix and embedded magnetic cobalt nanowires. We suggested hard magnetic cobalt nanowires in robot fabrication to avoid the use of high-cost rare-earth materials and achieve comparable magnetic characteristics. For the elastomer matrix, we chose Ecoflex, which is widely used in diverse areas of soft robotics and medical fields because of its excellent biocompatibility and stretchability.[51]

The specially developed procedure of cobalt nanowires synthesis was employed based on the previously obtained method by Mohapatra et al.[52] The method of synthesis of Co nanowires involves the solvothermal reduction of cobalt(II) laurate (4.5 mM) by 1,2-butanediol (Figure 2A). Hexadecylamine (2.4 mM) has the main role in nanowire formation and acts as a capping agent. Ru(III) (0.019 mM) was employed as a nucleating agent and allows the nucleation rate to be much higher than the metal growth rate.[53] Figure 2 presents details on the characterization of obtained magnetic Co nanowires. The morphology and structure of magnetic particles were examined by using scanning electron microscopy (SEM) and transmission electron microscopy (TEM). The SEM image shows a large quantity of wire-like nanostructures (Figure 2B). According to TEM observation (Figure 2C), the mean size of the length and width of each nanowire is 850 and 17 nm, respectively. The crystalline structure of the product and its purity were

https://doi.org/10.1021/acsnano.2c10127
ACS Nano 2023, 17, 20925−20938

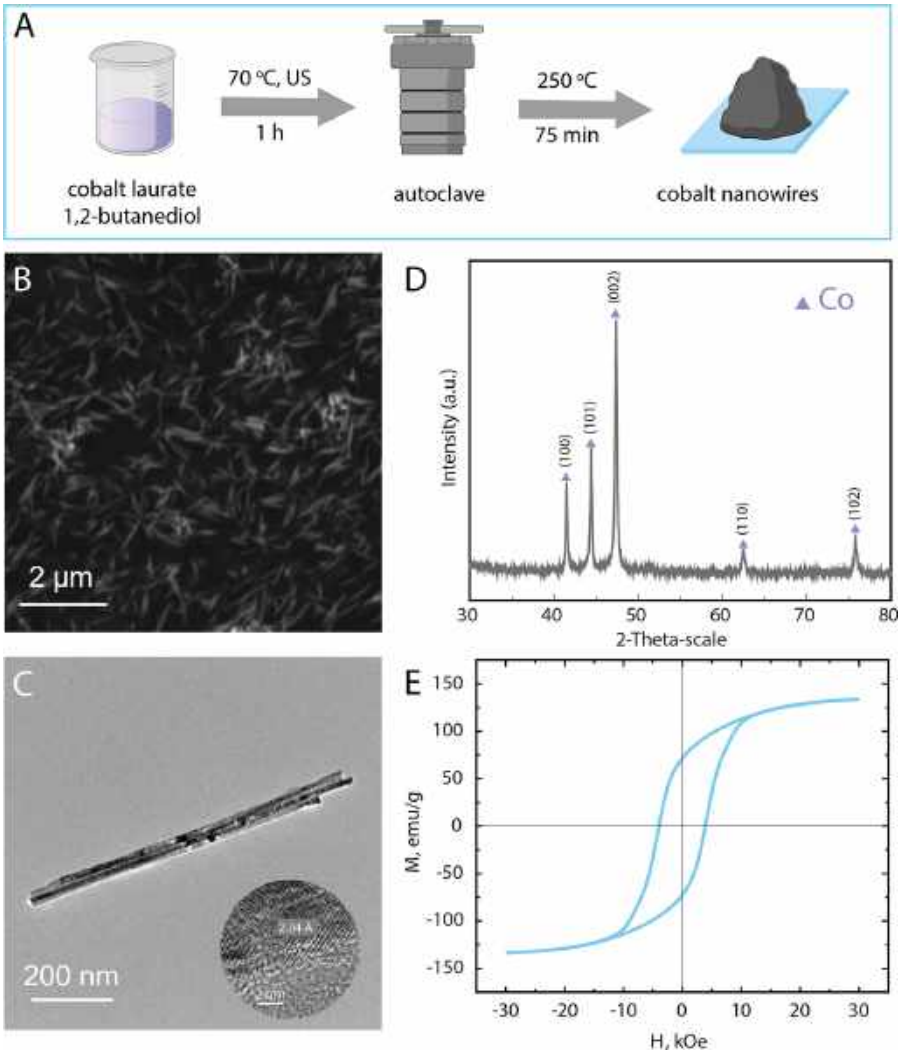

Figure 2. Structural characterization of obtained particles. (A) Synthetic procedures for obtaining cobalt nanowires. (B) Scanning electron microscope (SEM) picture of synthesized particles. (C) Transmission electron microscopy (TEM) picture of synthesized Co nanowires. Inset: high-resolution TEM image of a single Co nanowire. (D) X-ray diffraction (XRD) patterns of synthesized Co particles. (E) Room-temperature magnetic hysteresis loop (SQUID) of the cobalt nanowires.

determined by X-ray diffraction (XRD) (Figure 2D). The five diffraction peaks at 2θ values of 41.57°, 44.27°, 47.35°, 62.52°, and 75.77° corresponding to the crystal planes of (100), (101), (002), (110), and (102), respectively, can be observed. All the diffraction peaks can be well indexed to hexagonal-phase (hcp) cobalt with a fringe spacing of 2.04 Å, calculated by Bragg's formula, which corresponds to the literature.[54] A more detailed study of the magnetic nanowires was conducted by high-resolution transmission electron microscopy (HRTEM), recorded near the edge of the cobalt nanowire. The lattice spacing of 2.04 Å corresponding to the separation of the (002) planes of hexagonally packed cobalt is shown in the inset of Figure 2C; it also demonstrates that the nanowire is single-crystalline.

The magnetic properties of the obtained samples were measured using a superconducting quantum interference device (SQUID) magnetometer. The magnetic hysteresis loops at room temperature are shown in Figure 2E. The SQUID analysis shows well-pronounced ferromagnetic behavior for the sample with a large coercivity (3900 Oe), saturation magnetization (134.1 emu/g), and remnant magnetization (71.85 emu/g). A small decrease in saturation magnetization is observed compared to bulk Co (159.78 emu/g),[55] which is attributed to the presence of residues of the organic phase or partial surface oxidation.

Next, we modeled the robot structure evolution (Figure 3A) to understand the role and effectiveness of the robot shape during biofilm removal. From the starting point, we chose the 2D plane robot as a reference for the simplest shape, which could be found in numerous scientific papers. Then we imagined starting to roll the 2D robot into the 3D cylindrical shape. Cylindrical shape could also be a source of reference shape, as it corresponds to urethral catheter shape. By deforming the walls of the cylindrical robot, the influence of sharpness was observed in the form of a triangular shape. The evolution of triangle robots was achieved through quadratic shape via triangle twinning and rhombic (vane) robots via triangle twinning and rotation. The vane-like robot served as a starting point for the further sharp evolution of 5- and 8-pointed stars (denoted as star and octagram, respectively). The rationale for using star-shaped robots was based on a previous paper[42] that suggested sharper forms have a higher mechanical contact for effective biofilm cleaning. A robot size of 4.5 × 15 mm was chosen because it

https://doi.org/10.1021/acsnano.2c10127
ACS Nano 2023, 17, 20925−20938

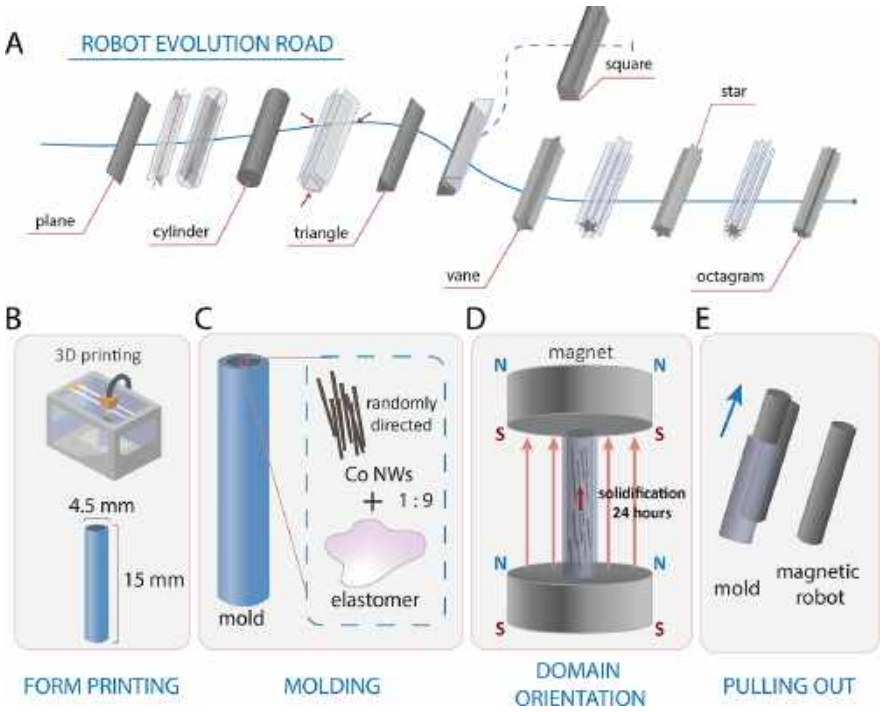

Figure 3. Robot evolution and fabrication. (A) Robot evolution from a simple 2D plane robot to star (5-pointed) and octagram (8-pointed); (B) 3D printing of a mold with suitable size for a 20 Fr catheter; (C) schematic illustration of the molding process; (D) curing of the composite in a mold under the action of the magnetic field; (E) pulling out the robot from the mold after curing.

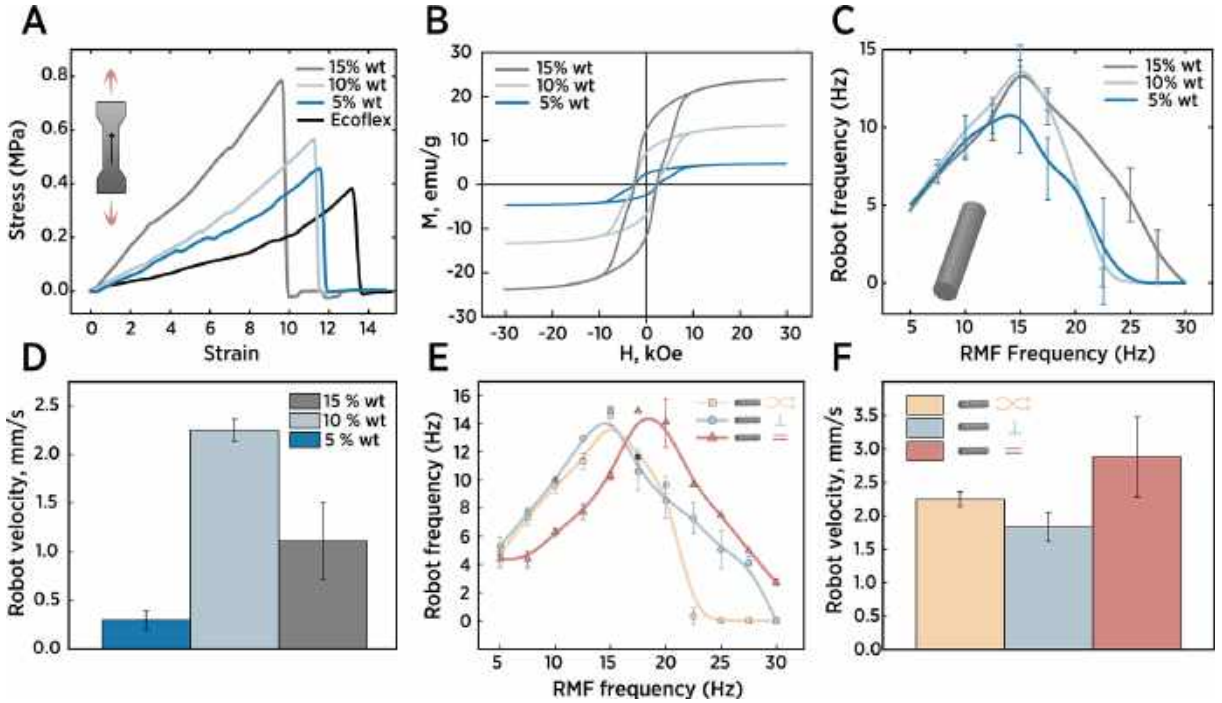

Figure 4. Magnetic robot behavior characterization. (A) Composite mechanical testing. Black arrow shows the magnetization direction of the composite. (B) Room-temperature magnetic hysteresis loop of the composite with the particle concentration at 5, 10, and 15 wt %. (C) The rotating frequency of robots with different weight ratios in regard to the external RMF frequency. (D) The velocity of robots with different weight ratios with regard to the external RMF frequency. (E) The rotating frequency of robots with different nanowire orientations with regard to the external RMF frequency. (F) The velocity of robots with different nanowire orientation with regard to the external RMF frequency.

corresponds to one of the most common male catheter sizes (20 Fr with an inner diameter of 5.1 mm).[50]

The next step of the research was robot fabrication and characterization to optimize its mechanical and magnetic properties for biofilm cleaning. We fabricated the robots via a 3D printer-assisted molding. In the first stage, we obtained polylactic acid (PLA)-based plastic hollow molds with the desired shapes of the future robot (Figure 3B). Next, robots

https://doi.org/10.1021/acsnano.2c10127
ACS Nano 2023, 17, 20925−20938

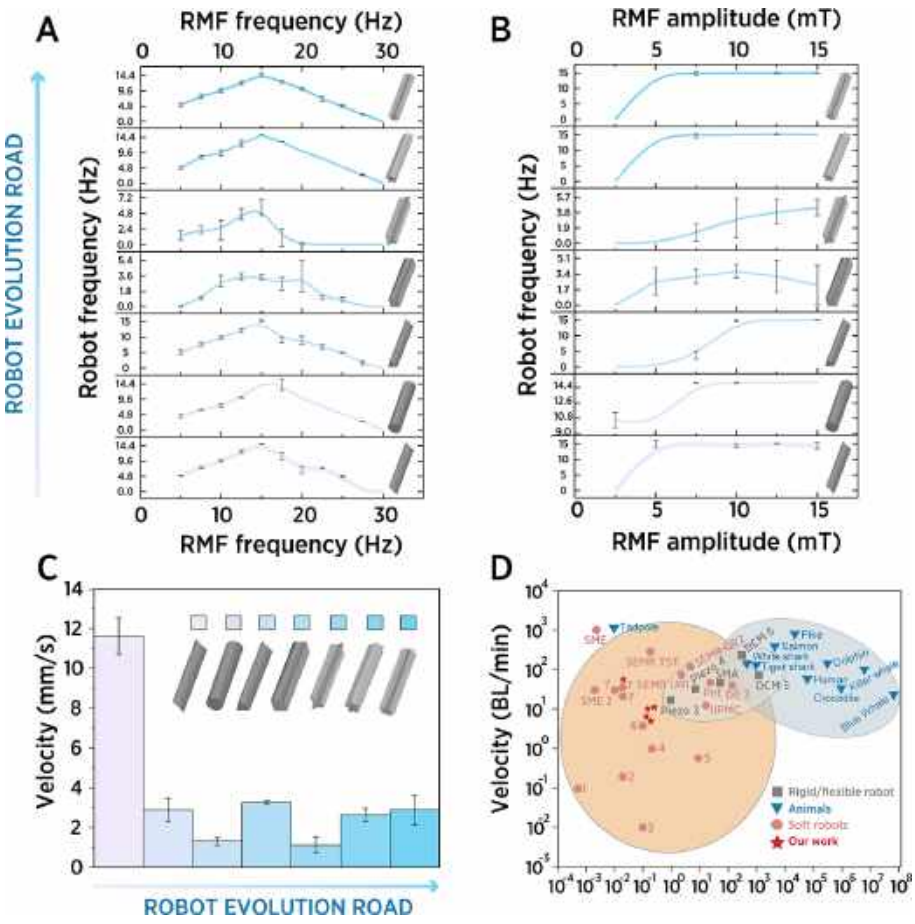

Figure 5. The frequency−amplitude analysis of magnetic soft robots under the action of RMF. (A) Analysis of robot rotation frequency regarding the external RMF frequency and fixed amplitude (10 mT). (B) Analysis of robot rotation frequency regarding the external RMF amplitude and fixed frequency (15 Hz). (C) Velocity of the robot under the action of RMF for all designed shapes. (D) Summary of the velocity performances of organisms and artificial soft and rigid robots.

were fabricated by mixing a certain amount of cobalt nanowire powder with silicon elastomer, filling the molds with this mixture, and curing it for 30 min at 60 °C (see Figure 3C). Importantly, the curing of the magnetic robots took place in the magnetic system (Figure 3D and Figure S1) to achieve both the orientation and magnetization of nanowires inside the elastomers. After cooling to room temperature, the solid composites were peeled off from the molds for further characterization (Figure 3E) (see the Methods Section: Composite Preparation for details).

To study the mechanical properties of the robots, uniaxial tensile tests of the composites with different cobalt nanowire weight fractions were performed on a mechanical testing machine (Figure 4A). Stress−strain curves clearly show the tendency of the tensile strength of the composite to increase (from 0.4 MPa for Ecoflex (0 wt %) to 0.8 MPa for the 15 wt % magnetic composite), while the stretchability falls from 139.65 ± 8 mm of extension for Ecoflex to 97.7 ± 17 mm for the 15 wt % magnetic composite. The increase in stress is attributed to particle-mediated reinforcement of the elastomer matrix with respect to the magnetic filler concentration.[56]

Further, the magnetic properties of the composites were studied by SQUID magnetometry (Figure 4B). The room-temperature magnetic hysteresis loops for composites with 5%, 10%, and 15% weight fractions show well-pronounced ferromagnetic properties with hard magnetic behavior with large coercivity (3 kOe for all samples), remanence (2.42, 7.11, and 12.37 emu/g for 5, 10, and 15 wt %, respectively), and saturation magnetizations (4.72, 13.34, and 23.8 emu/g for 5, 10, and 15 wt %, respectively). The decrease in the magnetic characteristics compared to the particle is attributed to the presence of elastomer matrices that cover the particles.

The next stage of robot characterization was to understand the robot's behavior in the presence of a rotating magnetic field (RMF). The experimental setup included the silicon tube, filled with water, and three pairs of axially positioned Helmholtz coils, which created the rotating magnetic field. To estimate the required composition for maximizing the magnetic actuation performance, the robots with different weight fractions of cobalt nanowires were investigated in the presence of the RMF (Figure 4C and Movie S1). For this study, we chose the cylindrical shape as the simplest form of the magnetic robot, which also remains an initial building block for robot evolution. The analysis of the three different robot compositions reveals similar behavior with different maximums of the robot frequency and identical step-out frequency: the robot with 5 wt % shows the maximum at 11.3 ± 3.1 Hz, while the 10 and 15 wt % have an equal maximum at 14.6 ± 0.7 and 14.5 ± 0.8 at 15 Hz and 10 mT of external RMF, respectively. The analysis of robot velocity with different weight fractions (Figure 4D) reveals a significant difference between robots (0.29 ± 0.09 and 1.1 ± 0.39 mm/s for robots with 5 and 15 wt %, respectively), with the highest speed value for the robot

https://doi.org/10.1021/acsnano.2c10127
ACS Nano 2023, 17, 20925−20938

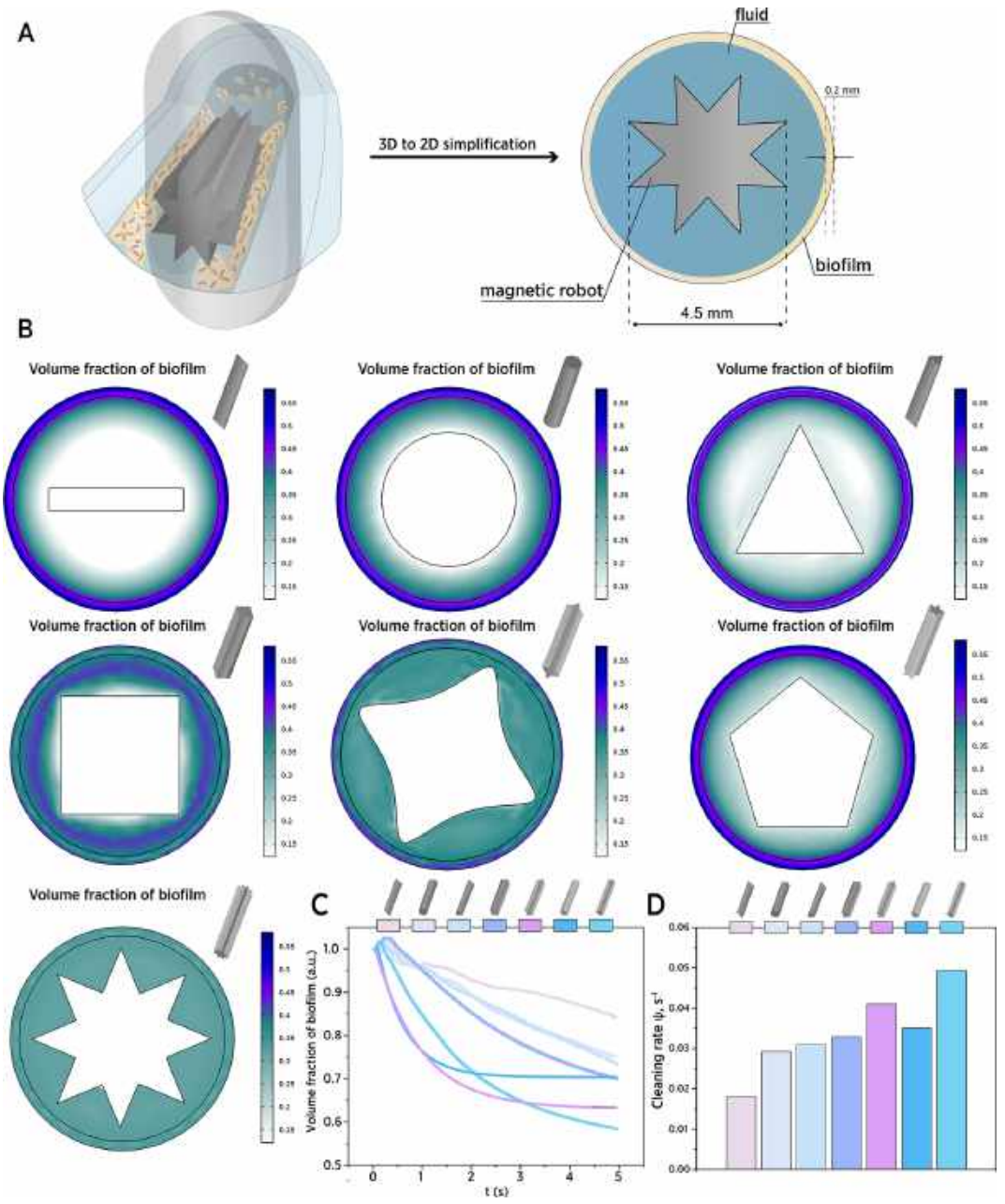

Figure 6. Multiphysical modeling of biofilm removal by the magnetic soft robot. (A) Geometrical features of the model, (B) 2D surface of the volume fraction of the biofilm after 1 s of magnetic soft robot rotation, (C) plot of the volume fraction of the biofilm with respect to the time and type of magnetic robot, and (D) cleaning rate ψ for different robot shapes.

with 10 wt % (2.25 ± 0.1 mm/s). The decrease in robot speed with increasing of magnetic particle content for 10 and 15 wt % could be explained by a dimensionless parameter, $\frac{MB}{G}$ (where M is magnetization (A/m), B is magnetic flux density (T), and G is shear modulus (Pa)), which characterizes the competition or balance between the magnetic interaction and the elasticity of the composite[44] (Figure S2). The ratio reached its maximum at 10 wt % ($\frac{MB}{G} = 5.88$), decreased at 15 wt % ($\frac{MB}{G} = 4.15$), and reached its minimum at 5 wt % ($\frac{MB}{G} = 1.98$).

To identify the plausible nanowire orientation within the robot, we constructed the magnetic system based on the two cylindrical magnets (NdFeB N52, 55 mm in diameter, 25 mm thickness) and magnetized the robot during elastomer curing in three different ways: parallel to magnetic field lines (denoted as ||), perpendicular (denoted as ⊥), or as-prepared cobalt nanowires were mixed with elastomer without magnetic field-assisted curing (denoted as crossed wavy arrows) (Figure 4E and Movie S2). We observed a slight change in the robot's mechanical properties for robots with different nanowire orientation, which could be attributed to the relative orientation of nanowires to the direction of stretch on the testing machine (Figure S3). The testing of these robots under RMF revealed that the parallel orientation of nanowires shifts the step-out frequency of the robot from 15 Hz (for random and perpendicular orientations) to 20 Hz with the maximum rotating frequency between 17.5 and 20 Hz of the actuation field. Interestingly, the robot frequency with random orientation drastically fell after 20 Hz, while the perpendicular and parallel

https://doi.org/10.1021/acsnano.2c10127
ACS Nano 2023, 17, 20925−20938

orientations had a slower tendency to decrease the rotating number. The velocity analysis shows (Figure 4F) the highest speed for the robot with a parallel orientation (2.88 ± 0.59 mm/s) compared to random and perpendicular orientations (2.25 ± 0.11 mm/s, 1.84 ± 0.22 mm/s). The evidence of asynchronous and oscillation mode changes after the step-out frequency point proves the different orientations of the nanowires inside the robot. Taken together, we choose 10 wt % as the optimal robot composition with parallel nanowire orientation based on the key magneto-mechanical property: the highest robot frequency and velocity under RMF with an excellent actuation range with comparable rotation frequency values with the robot with a bigger particle weight ratio.

Next, we studied the behavior differences between the presented designs of magnetic soft robots under the action of RMF (Figure 5 and Movie S3). First, frequency−amplitude analysis was performed to estimate the possible characteristic changes during the shape evolution of the robots (Figure 5A,B). Surprisingly, only square-shaped and vane-like robots show a significant difference compared to other shapes (Figure 5A). Specifically, the maximum of robot rotating frequency for a vane-like robot was 5.75 ± 1.28 at 15 Hz of external RMF, the square-shaped robot shows a broad maximum with minor changes of ca. 3 ± 0.8 Hz in the range 10−20 Hz of RMF, while the other forms reached a maximum at ca. 15 Hz at 15 Hz of RMF. The amplitude analysis of all forms (Figure 5B) shows the rapid increase of robot rotation frequency to the maximum (ca. 5 mT of external RMF amplitude) for the plane, cylinder, and 5,8-pointed stars, while the square and vane robots show a broad maximum of robot frequency and slowly increase to a maximum at 15 mT, respectively.

The obtained data for the velocity of the magnetic robot are shown in Figure 5C. Despite the plane robot with significantly lower weight (11.6 ± 0.9 mm/s), the other forms showed the velocity in the following range: square (3.255 ± 0.1 mm/s) > 8,5-pointed star and cylindrical robots (2.88 ± 0.6 mm/s) > triangle and vane robots (1.3 ± 0.19 mm/s and 1.1 ± 0.41 mm/s). The effectiveness of the velocity performance of these magnetic robots could be clearly seen by comparing their normalized velocity against the body mass of reported soft robots, semiflexible robots, and animals (Figure 5D and Table S1). The developed 3D magnetic robots showed a medium swimming efficiency (11.52 BL/min for cylinder, 13.02 BL/min for square, 11.55 BL/min for octagram) comparable to some semiflexible robots (18 BL/min for Piezo 3,[57] 12 BL/min for ionic polymer−metal composites)[57] and higher than 58% of reported soft robots. At the same time, the plane 2D robot (46.45 BL/min) shows a comparable swimming efficiency with animals (crocodile (30 BL/min), whale (24 BL/min), most semiflexible robots and soft robots (DE 3 (42 BL/min),[58] Piezo 4 (48 BL/min), pneumatic (48 BL/min)),[59] and shape memory-based robots (48 BL/min).[60] The difference in the robots' velocities with distinct cross sections is associated with the difference between tangential and normal drag coefficients,[61] which, in the case of sharp corners with wide space between them, allows breaking the interface of the laminar flows for efficient self-propulsion, which is similar to previous research.[62] In contrast, cylinder robots and 5,8-pointed stars have a smooth surface, which is favorable for moderate self-propulsion, while triangle and vane-like robots have an asymmetric design and a smaller corner-to-corner distance, which is undesirable.

Prior to experimental validation of the proposed concept of biofilm removal, we employed multiphysical modeling to understand the efficiency of magnetic soft robot designs and study the possibility of biofilm removal by the fluid shear stress generated through robot rotation under the action of the RMF (Figure 6). The phase-field model found a special place for the modeling of the biofilm deformation[63−65] and was used in this work. The biofilm was assumed as a continuum shell around the catheter boundary with a 0.2 mm thickness, which was based on the literature data for a 3-day biofilm thickness.[66] The frequency of rotation for a magnetic soft robot with the desired design was consistent with the experimental results from Figure 5. The modeling was implemented using COMSOL Multiphysics 6.0 (COMSOL Inc., Burlington, MA, USA). The results of multiphysical modeling are summarized in Figure 6.

Figure 6B shows the 2D surface of the biofilm volume fraction after 1 s of the magnetic soft robot rotation. The evolution tendency for faster homogenization of the biofilm by the robots is clearly visible. While the plane and cylinder robots show smaller biofilm detachment, the forms with sharper corners, such as square, vane, star, and octagram, could perturb the biofilm−fluid interface and, consequently, provide sufficient shear stress for biofilm detachment, reaching an almost isotropic solution for the octagram robot. Furthermore, the dynamics of biofilm detachment highlight the superiority of sharper forms. This is evidenced by the exponential decrease in biofilm volume fraction compared to smoother forms, which exhibit nearly linear behavior (Figure 6C). For quantitative comparison of the different robot shapes, we introduce the cleaning rate, which is defined as $\psi = \frac{\Delta\varphi}{\Delta t}$, where $\Delta\varphi$ is the biofilm volume fraction difference at the start and end point of modeling and Δt is the running model time. Figure 6D shows almost linear growth of the cleaning rate during robot evolution. The smaller values are for the plane and cylinder (0.018 and 0.029 s^{-1}), while the moderate values are for the first sharp evolution variants, triangle (0.031 s^{-1}), square (0.033 s^{-1}), and star (0.035 s^{-1}), with dominance of the vane (0.041 s^{-1}) and octagram (0.049 s^{-1}) robots as the most promising robot shapes for biofilm eradication.

The principal experiment for the efficacy understanding of the developed concept is an evaluation of biofilm removal from the catheter by magnetic soft robots. Based on the results from the previous section, the optimized magnetic field parameters include a 10 mT amplitude and a 15 Hz frequency (Figure 6A). The urethral 20 Fr catheter was employed as an exemplary system to model biofilm growth during patient treatment. The *P. aeruginosa* and *S. aureus* were used as typical microorganisms that could be found on the catheter surface.[8] Briefly, biofilms were grown in the urethral catheters for 3 days and stained with crystal violet to estimate the biofilm removal efficiency by spectrophotometry. The procedure for catheter cleaning using a magnetic robot was as follows: robots were inserted through the balloon port of the catheter; after that a rotating magnetic field drives the robots in an upward movement for catheter biofilm eradication. The removal of the robot was done by downward motion driven by a rotating magnetic field and the use of a permanent magnet to extract the robot from the catheter through the balloon port. In the case of the robot adhering to the catheter surface, the use of a small gradient magnetic field allows it to unstick the robot from the surface. Bearing in mind the numerous applications of the magnetic actuator for biofilm removal, the cobalt nanowire swarm was also included in the cleaning demonstration.

https://doi.org/10.1021/acsnano.2c10127
ACS Nano 2023, 17, 20925−20938

Movie S4 and snapshots in Figure 7B show the biofilm removal from the catheter surface during 1 min of magnetic field application. Specifically, under the action of RMF, the magnetic torque drives the robots in an upward movement, causing hydrodynamic shear stress to address the main task to eliminate biofilm. The results of biofilm removal are summarized in Figure 7C and D. The Gram-negative *P. aeruginosa* biofilm (Figure 7C) shows low resistance to magnetic robot cleaning and could be completely removed by the simple cylinder. Notice that the efficiency of catheter cleaning correlates with the robot evolution direction and reached almost full cleaning level for the star and octagram. The most inefficient robots were the 2D plane (72.4 ± 10%) and square (70.71 ± 5.9%), which in turn proves the major role of shape and surface sharpness. In the case of the stiffer and biochemically different Gram-positive *S.aureus*, the biofilm of that type shows much greater resistance to removal by the magnetic soft robot (Figure 7D). Particularly, only the octagram and star robots reached high biofilm cleaning (88.8 ± 5.53% and 71.3 ± 4.9%) with a clear trend following the proposed shape evolution model: the 2D plane and cylinder were inefficient (50.7 ± 8.78% and 55 ± 7%, respectively), the triangle showed 48.3 ± 9%, an almost linear growth of efficacy was seen for further evolution variants square and vane-like (63.52 ± 10% and 61.38 ± 7.1%), and the two champions were the star and octagram. Notice that the robot's integrity does not provide any chance of toxicity after biofilm treatment, while the cobalt nanowires have a significant dangerous pattern on the human cell line (Figure S4). These data are also in good agreement with the results of multiphysical modeling with superior efficacy of octagram-shaped robots with a linear increase of effectiveness for other forms according to the evolution rule (Figure 6). Specifically, if we normalize the data by octagram efficacy (real biofilm eradication efficiency for experimental data and cleaning rate for modeling data), we saw the modeling underestimation for the plane and star robots (20% and 27.9% underestimation), while for other shapes, it shows a good compliance (Figure S5). The reason for this could be found in the 2D simplification of the modeling, which does not show the influence of the motion velocity of the robots and inaccuracy in the robot fabrication compared to the ideal geometrical model. It is important to note that the demonstrated results were achieved on part of a catheter (5 cm long) compared to the clinical size (20−40 cm) due to the limited magnetic field workspace (60 × 13 mm chamber). For the translation of the developed concept, building a clinically relevant magnetic setup would be beneficial.[67,68]

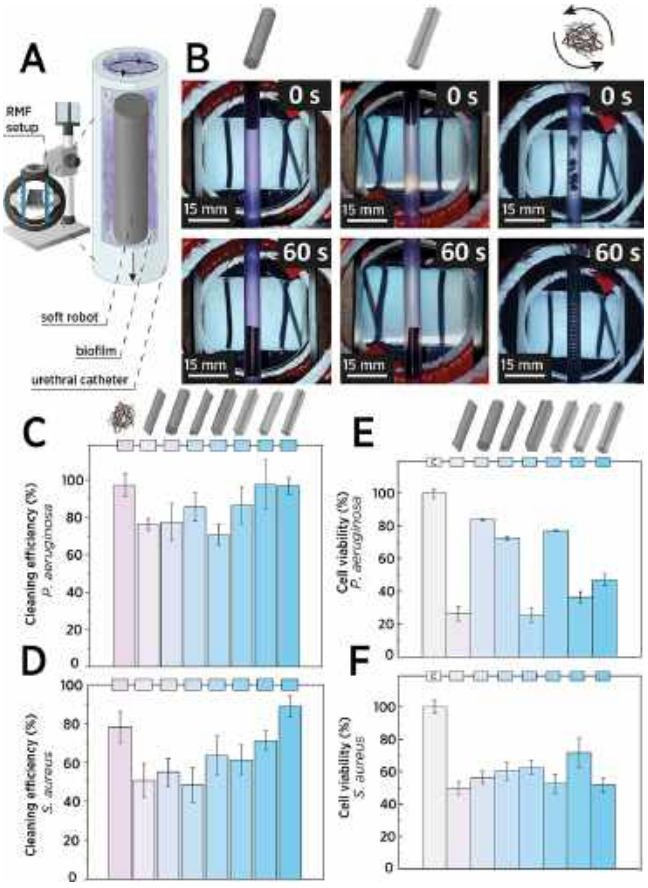

Figure 7. Biofilm eradication experiment. (A) Experimental setup. (B) Snapshot of the robot and nanowire swarm movement inside the catheter during biofilm eradication (C) Robot and swarm cleaning efficiency of *Pseudomonas aeruginosa* biofilm. (D) Robot and swarm cleaning efficiency of *Staphylococcus aureus* biofilm. (E) Viability of the *P. aeruginosa* bacteria after cleaning by the robots. (F) Viability of the *S. aureus* bacteria after the cleaning by the robots was studied; the control experiment was designated as the symbol "C".

The assessment of bacteria viability after the biofilm removal is essential due to the risk of inflammation caused by biofilm debris and to prevent bacteria regrowth within the catheter. Figure 6E and F show the capability of the magnetic robots to eradicate bacteria after biofilm removal. The Gram-negative *P. aeruginosa* biofilm (Figure 7E) has relatively low viability after treatment by the 2D plane (26.3 ± 4.7%), square (25.2 ± 4.3%), star (36.3 ± 3.5%), and octagram-shaped robots (47 ± 3.49%). The Gram-positive *S. aureus* demonstrated an almost shape-independent inactivation and higher viability at a minimal level after the 2D plane (49.8 ± 4%) and octagram robot (51.8 ± 4.2%) treatment, which could be explained by the stiffer cell wall of the *S. aureus* over *P. aeruginosa*. These results show the potential of the developed magnetic soft robot to remove and partially inactivate bacteria biofilm to increase the lifetime of catheters during clinical treatment. To avoid biofilm regrowth and inflammation after the biofilm removal, we believe that the use of our robot as a part of medical devices (e.g., ureteroscopy endoscope) capable of adsorbing and retrieving physiological liquids with biofilm debris would be beneficial.[69] The most plausible mechanism of partial bacterial inactivation for the more sensitive *P. aeruginosa* is a sufficient wall shear stress gradient in the case of the robots with higher velocity: 2D plane robot (cell viability 26.3 ± 4.7%) and square robot (cell viability 25.2 ± 4.3%), while their biofilm removal efficiency is moderate since lower velocity is beneficial for removing the adhered biofilm. Similar results could be found in ref 69, where the partial bacteria inactivation was achieved by a rotating helical micromachine even without an antimicrobial compound (H_2O_2), although the H_2O_2 (1%) significantly improved the biofilm eradication.

Our next step was dedicated to understanding the clinically relevant points of the developed concept, such as efficiency of biofilm eradication toward a thicker 7-day-grown biofilm (Figure 8A (i)), a comparison of the magnetic robot with biofilm removal by a urogenital brush (Figure 8A (ii)), the possibility of robot reusability (Figure 8A (iii)), and assessment of magnetic soft robot efficacy for catheters of different sizes (Figure 8A (iv)). For these points, we chose the octagram-

https://doi.org/10.1021/acsnano.2c10127
ACS Nano 2023, 17, 20925−20938

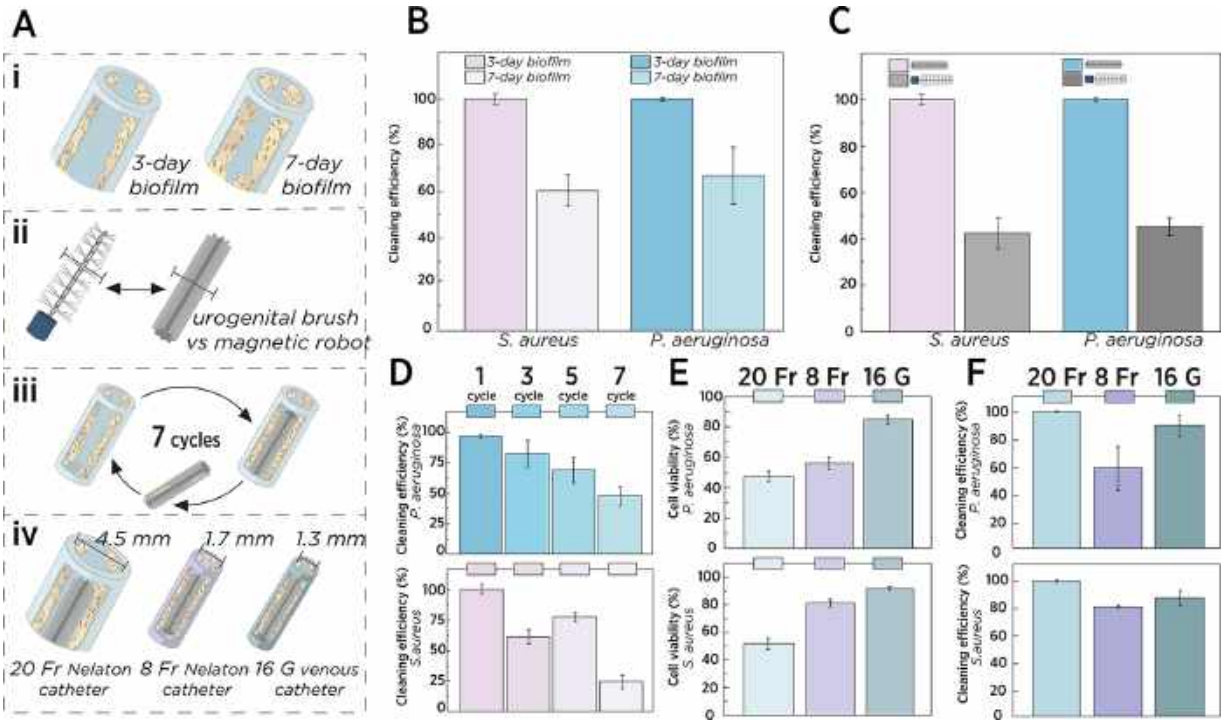

Figure 8. Advanced biofilm eradication experiments. (A) (i) cleaning of 7-day-grown biofilm by a magnetic soft robot, (ii) comparison of the robot efficacy with a urogenital brush, (iii) recyclable biofilm cleaning from the catheter surface by a magnetic soft robot, (iv) cleaning of the biofilm from the catheters of different sizes. (B) Octagram-robot cleaning efficiency of *Pseudomonas aeruginosa* and *Staphylococcus aureus* 7-day-grown biofilms. (C) Octagram-robot cleaning efficiency of *P. aeruginosa* and *S. aureus* biofilms compared to cleaning with a urogenital brush. (D) Octagram-robot cleaning efficiency of *P. aeruginosa* and *S. aureus* biofilms during 7 cycles. (E, F) Octagram-robot cleaning efficiency of *P. aeruginosa* (E) and *S. aureus* (F) biofilms from catheters with different inner diameters: 20 Fr (4.5 mm), 8 Fr (1.7 mm), and 16 G (1.3 mm).

shaped robot as the most effective shape for biofilm removal and one of the most effective for bacteria inactivation.

First, we studied the efficacy of an octagram-shaped robot against the thicker shell of a 7-day-grown biofilm, which is the upper limit of indwelling catheter wearing (for example, Coloplast catheters) (Figure 8B). We observed an almost 2-fold decrease in efficiency compared to almost full eradication of the 3-day biofilm eradication (60.5 ± 6.76% and 67 ± 12% for *P. aeruginosa* and *S. aureus* 7-day biofilms, respectively). To increase the biofilm removal in the case of the 7-day biofilm, we increased the number of robot loads from 1 to 4 and achieved 78.8 ± 6.63% biofilm removal for *S. aureus* (Figure S6). The complete removal of the 7-day biofilm could be achieved by the backward motion of the magnetic soft robot during a longer time of treatment.

Further, we provide a useful comparison of the developed magnetic soft robot with the cleaning efficiency of a simple urogenital brush, intensively powered by the author's hand (Figure 8C). Surprisingly, the urogenital brush had a much lower biofilm removal efficiency compared to the octagram-shaped robot (42.65 ± 6.7% and 45.4 ± 3.96% for *P. aeruginosa* and *S. aureus* biofilms, respectively). The reason for this could be found in the viscoelastic solid−fluid properties of biofilm;[70] the bristles of the brush actuate the biofilm surface with a much lower loading rate compared to almost 15 vibrations per second for magnetic soft robots. The high load could induce instabilities at the fluid−biofilm interface and drive biofilm detachment from the catheter surface, which is similar to the work of high-velocity microsprays for biofilm mechanical cleaning.[71,72]

Next, the reusability of the octagram-shaped robot was assessed by using one particular robot for biofilm eradication during seven cycles of removal (Figure 8D). We observed a gradual fall in biofilm cleaning efficiency, reaching the minimal level at 24.4 ± 5.38% and 47.36 ± 7.7% for the removal of *P. aeruginosa* and *S. aureus* biofilms during the seventh cycle, respectively. Nevertheless, good reusability of the octagram robot was found during three cycles of *P. aeruginosa* biofilm removal (81.8 ± 10.8%) and two cycles of *S. aureus* (74 ± 10.1%) biofilm removal. The reason for the efficiency decrease could be found in the biofilm's attachment to the robot's surface after the eradication and possibly might be improved by extracting bacteria from the robot.

Finally, the relevance of the magnetic soft robot for biofilm removal from catheters with different sizes was assessed, including urinary catheters with 20 Fr (4.5 mm) and 8 Fr (1.7 mm) sizes and a venous catheter of 16 G (1.3 mm). For this experiment, the magnetic robot size was downscaled to correspond to catheters with similar behavior under the application of a rotating magnetic field with higher velocity for the mini-robot (for an 8 Fr catheter) and microrobot (for a 16 G catheter) (Figure S7). A significant decrease in the robot's efficiency was observed with decreasing size for bacteria inactivation efficiency (Figure 8E) and a slight decrease for biofilm removal (Figure 8F). These results suggest using the developed magnetic soft robot for catheters with larger sizes, while smaller ones require optimization of the magnetic field mode and treatment time to ensure full biofilm removal.

To understand whether the magnetic soft robot could damage the wall of catheters with an antimicrobial surface, we used a commercially available antimicrobial Foley catheter, which was cleaned by a robot under the application of a magnetic field, and after that the biofilm formation was assessed. We found no

https://doi.org/10.1021/acsnano.2c10127
ACS Nano 2023, 17, 20925−20938

significant difference in biofilm growth between antimicrobial catheters with and without robot cleaning (Figure S8). From these results, we can conclude that our robot is safe for application with antimicrobial catheters without any reduction in the antimicrobial capability. We observed some biofilm formation (approximately 3 times larger formation of biofilm in a regular catheter) mainly due to mismatch in culture growth in the laboratory and naturally in the patient's body.

Taken together, these findings show the significance of the robot shape for biofilm elimination, and future studies should focus on preclinical and clinical evaluation of the presented concept for minimally invasive biofilm removal from relatively large catheters. The integration of the developed magnetic soft robot with medical devices is also suggested to ensure the elimination of biofilm debris from the catheter lumen after treatment. It should be noted that the magnetic nanowire swarm also showed a superior efficiency toward the biofilm elimination (97.22 ± 6.15% for *P. aureginosa* and 78.27 ± 8% for *S.aureus*). The main limitations of swarm application are higher toxicity (Figure S3), infiltration in silicone catheters (Figure S9), and possible accumulation in human organs. In turn, the magnetic soft robot provides a biosafe and reusable alternative approach for biofilm treatment.

CONCLUSION

In this paper, we proposed a strategy to remove the biofilm on the catheters' surface by a magnetic soft robot driven by a rotating magnetic field. First, we suggested a set of shapes with a clear evolution line to assess the biofilm removal efficacy and found the most efficient shape. Next, we optimized the composition of the robot and studied the robot's behavior under the action of a rotating magnetic field with precise investigation of frequency, amplitude, and shape dependencies of behavior. Prior to the experimental validation, we predicted the cleaning efficiency for the set of magnetic soft robots against biofilm. We found the benefit of the sharper robot designs for biofilm eradication and highlighted the superior efficiency of the octagram-shaped robot. Finally, we studied the biofilm removal efficiency and bacteria viability on clinically relevant urethral catheter models and bacteria strains. We found the octagram-shaped robot to be the most plausible design for complete biofilm removal from the catheter surface, which also correlates with multiphysical prediction. We demonstrated the capability of magnetic robots to partially inactivate the bacteria after the biofilm removal. We also assessed the reusability of the octagram robot and biofilm removal of the thicker 7-day biofilm and compared the effectiveness of the magnetic soft robot and urogenital brush. We found the octagram-shaped robot was twice as effective as a mechanical urogenital brush (96.85 ± 4.45% and 88.8 ± 5.53% of eradication for the robot vs 42.65 ± 6.7% and 45.4 ± 3.96% for *P. aeruginosa* and *S. aureus* biofilms eradication by the brush, respectively). The developed magnetic soft robot also showed a good efficiency of the biofilm removal (56 ± 1.65% and 84.3 ± 3.1% for *P. aeruginosa* and 81 ± 2.6% and 91 ± 1.5% for *S. aureus* on 8 Fr and 16 G catheters, respectively) from the catheters with a smaller size (8 Fr (1.7 mm) and 16 G (1.3 mm)). We also demonstrated the relevance of the developed concept for biofilm removal from catheters of different sizes. Our approach for biofilm treatment could not only decrease the number of HAIs but also improve the patient's comfort during long-term catheterization, especially for people over the age of 65. The introduction of minimally invasive biofilm removal from catheters on a hospital scale could decrease the additional cost due to the number of catheters needed and reduce recycling costs. For the preclinical and clinical translation of the developed concept, building a human-scale magnetic setup would have significant importance, which could include a robotic arm with a rotating permanent magnet for sufficient RMF conditions for magnetic soft robot applications. We anticipate the integration of a soft magnetic robot with a semiflexible medical device, which could increase the effectiveness of the biofilm eradication, would be reliable for clinical applications. This finding could play a crucial role toward the treatment of biofilm-associated catheter contamination with possible applications for urethral, central venous, and gastrostomy catheters.

METHODS

Synthesis of Cobalt(II) Laurate. Cobalt(II) laurate, $Co(C_{11}H_{23}COO)_2$, was prepared following the procedure from a previously published synthesis.[73] Dodecanoic acid (8.81 g, 44.0 mmol) and NaOH (1.68 g, 42.0 mmol) were added to distilled water (40 mL) while being mixed using a mechanical stirrer (350 rpm). The mixture was heated to 60 °C until a clear solution was obtained; then 10 mL of an aqueous solution of $Co(NO_3)_2{\cdot}6H_2O$ (5.82 g, 20.0 mmol) was added dropwise into the solution. After a purple precipitate formed, the mixture was stirred and kept at 60 °C for 30 min. Finally, the precipitate was recovered with centrifugation (10 000 rpm for 10 min) and then was washed one time with distilled water and two times with methanol. After that it was dried in an air oven at 60 °C.

Magnetic Cobalt Nanowires Synthesis. The cobalt nanowires were obtained by optimization of a previously published synthesis.[52] Cobalt(II) laurate (2.07 g, 4.5 mmol), $RuCl_3$ (0.004 g, 0.019 mmol), hexadecylamine (0.58 g, 2.4 mmol), and 60 mL of 1,2-butanediol were introduced inside a Teflon enclosure (100 mL). The mixture was purged with Ar gas for 5 min. Next, the Teflon enclosure was placed in an ultrasonic water bath heated to 75 ± 5 °C for 60 min. After that, the enclosure was placed within a steel autoclave heated to 250 C in an oven. Then, after the temperature increase it was maintaining at 250 °C for 75 min. After cooling to room temperature, the black powder was centrifuged at 10 000 rpm for 10 min. The black powder was washed several times with *o*-xylene and gathered by an external magnet. Afterward, cobalt nanowires were dried at 50 °C and collected for the following characterization.

Characterization of Cobalt Nanowires. The obtained powder was characterized by SEM using a VEGA3 TESCAN scanning electron microscope. X-ray diffraction spectra were obtained on an Apex Duo (Bruker) at 1.5418 A (Cu Kα). The size of the cobalt nanowires and the features of their spatial distributions were studied by HRTEM. TEM images were obtained using a JEOL JEM-F200 microscope with an accelerating voltage of 200 kV, a cold field emission gun with a current of 12−15 μA, a 01361 RSTHB double-tilt Be specimen holder, and a CMOS AMT camera. Magnetic properties were measured on a VersaLab Quantum Design magnetometer.

Mold Preparation. Hollow molds of designed robot shapes with an aspect ratio of 25:7 mm were obtained using a FlyingBear Tornado 2 3D printer (China). Molds were printed from PLA plastic, and the 3D models for printing were created using the software Autodesk Tinkercad.

Composite Preparation. Co nanowires were mixed with a silicone elastomer (Ecoflex 00-30) in a 5%, 10%, and 15% weight ratio. To study the effect of nanowire orientation, the curing process took place inside the magnetic system. The composite mixtures were poured into molds and cured at 60 °C for 30 min. After the mixture was cooled to room temperature, the solidified composites were peeled off from the molds.

Composite Mechanical Testing. Soft composites with different Co nanowire weight fractions (0, 5, 10, and 15 wt % magnetic particles in the elastomeric matrix) were prepared by molding in dog-bone-shaped patterns with assigned dimensions (width, 5 mm; gauge length, 20 mm; thickness 0.8 mm). The molds were implemented by the milling cutter, for which the programming code was written using a

https://doi.org/10.1021/acsnano.2c10127
ACS Nano 2023, 17, 20925−20938

commercially available software package, ArtCAM 2008. The samples were tested on a mechanical testing machine (Metec, LS1) with a 20 N load cell at a strain rate of 0.01 s^{-1}; then stress−strain curves were obtained. The direction of the stretch of the composite material was related to nanowires aligning during fabrication.

Multiphysical Modeling. The modeling was implemented using COMSOL Multiphysics 6.0 (COMSOL Inc.). The dynamics of the biofilm−fluid interface was studied by the Phase Field modulus, and the fluid velocity and pressure were modeled using the Laminar Flow modulus. The geometry of the robot was based on the model for 3D printing of the molds, and the Form Assemble option was used to assess the robot's rotation. The Moving Mesh modulus was implemented for introducing the robot's rotation with the constant revolutions per time options. The biofilm and fluid dynamic viscosity were 10 and 0.001 Pa·s, respectively, while the mobility tuning parameter was set as 1×10^{-9} based on a previous paper.[64] For the plot in Figure 6C we obtained a volume fraction of biofilm data from the point on the middle center boundary of the biofilm domain. The data extraction for the snapshots in Figure 6B includes the final time frame of simulation (5 s) for each snapshot.

Rotating Magnetic Field Setup. A rotating magnetic field was created with the custom-built TOR 3D device (Nanomaterials, Russia). The magnetic system is composed of three pairs of axially positioned Helmholtz coils that can produce magnetic fields in different directions. There is a uniform field in each chamber with maximum magnetic flux density in the center of the experiment chamber of 15 ± 2% mT.

Biofilm Removal from Urethral Catheter by a Magnetic Soft Robot. Studies of the magnetic robot's effectiveness were carried out in an in vitro model using a Nelaton urethral catheter (the initial catheter was cut in parts of 5 cm). Biofilms were prepared by preincubating cell suspensions (10^6 cells/mL) in a growth medium on borosilicate glass slides and 96-well immunological plates at 37 °C for 3 and 7 days. After washing out the plankton cells, fresh growth medium, distilled water, and robots were placed inside the catheters to estimate the effectiveness. After testing in RMF with a 10 mT amplitude and a 15 Hz frequency, the catheters were prepared for quantitative analysis.

Quantitative Evaluation of Biofilm Removal. To quantify the biofilms, they were stained with 0.1% crystal violet. The dye bound to the biofilm was later extracted with a mixture of ethyl alcohol and acetone (9:1). The effectiveness of biofilm removal was evaluated by solution color intensity on a spectrophotometer at the wavelength of 600 nm (Agilent Cary 60).

Quantitative Evaluation of Bacteria Viability. To quantify bacterial viability, the live biofilm was treated by the magnetic robot in a Nelaton urethral catheter. After incubation, the growth media was removed from the catheters to wash out planktonic cells, and they were gently filled with 0.9% NaCl and the magnetic robots. When the treatment was carried out, the solution from the catheters was removed and washed with centrifugation 10000*g* for 10 min three times. A 3 μL solution of propidium iodide and Syto-9 mix was added and incubated with bacteria at room temperature in the dark for 15 min and washed one time with centrifugation at 10000*g* for 10 min. After staining, the bacteria cell was evaluated by fluorescent microscopy (a LEICA DMI8), and the number of live and dead bacteria was counted by ImageJ (NIH, USA).

Cytotoxicity Assay. The cytotoxicity of Co particles, elastomer matrix Ecoflex 00-30, and magnetic soft robots was assessed by the MTT method. HEK-293 cells were maintained in 96-well plates and incubated at 37 °C for 24 h.

For the MTT assay nine samples were prepared: the amount of magnetic particles required for fabrication of one whole robot, half a robot, and two whole robots (30, 15, and 60 mg of Co particles, respectively); one standard using robot, half a robot, and two whole robots; the amount of elastomer matrix (Ecoflex 00-30) required for fabrication of one whole robot, half a robot, and two whole robots (300, 150, and 600 mg, respectively). The octagram-shaped robot was used, considering that the highest plane amount could lead to the highest residue effect after further procedure performance. Every sample was disinfected before the experiment with isopropanol alcohol and irradiated under a UV lamp.

The experiment was conducted as follows. First, the specimen was put into the 5 mL falcons with 2 mL of culture media (DMEM, 10% FBS, 50 mg/mL gentamicin) in a sterile environment. Then, the falcon was inserted for 10 min in an RMF setup TOR 3D with adjusted parameters: 10 mT amplitude and 15 Hz frequency in the X and Z directions. The field characteristics were selected according to the robot motion behavior analysis. The procedure time corresponds to the approximate time of biofilm eradication for prospective in vivo experiments. After that, the samples were extracted from the falcons aseptically and the residuary culture media was centrifuged by a 5418 R centrifuge at 12 000 rpm for 5 min to avoid the presence of remaining particles or robot parts. Supernatant liquids were transferred to 96-well culture plates. Absorbance was registered at the 492 nm wavelength by a microplate reader Spark (Tecan), and the percentage of metabolic activity in each well was calculated relative to the absorbance of the control. Each sample had three repetitions for every cell incubation time period (24, 48, and 72 h).

ASSOCIATED CONTENT

Supporting Information

The Supporting Information is available free of charge at https://pubs.acs.org/doi/10.1021/acsnano.2c10127.

The magnetic flux density distribution for the magnetic system that was used for composite curing; experimental data of the ratio between magnetic and mechanical properties of the robot; robot mechanical testing with different nanowire orientation; cytotoxicity study of Co particles, magnetic soft robots, and the elastomer matrix Ecoflex by the MTT method; biofilm cleaning efficiency comparison for experimental data and modeling results, normalized by octagram-shaped robot efficiency; octagram-robot cleaning efficiency of *S. aureus* 7-day growing biofilm; frequency analysis of magnetic soft robots with different sizes under the action of RMF; study of the influence of the robot's movement inside the catheters on the antimicrobial capabilities of the inner surface of a catheter; cobalt nanowire swarm infiltration into the urethral catheter after biofilm eradication; comparison of the maximum swimming speeds of animals and robots (PDF)

Movie S1. Behavior of robots with different cobalt nanowire weight fractions in RMF (MP4)

Movie S2. Behavior of robots with different cobalt nanowire orientations in RMF (MP4)

Movie S3. Behavior differences between designs of magnetic soft robots in RMF (MP4)

Movie S4. Removing biofilm from catheter surface with cylindric robot, robot-octagram, and cobalt nanowire swarm (MP4)

AUTHOR INFORMATION

Corresponding Author

Vladimir V. Vinogradov − *International Institute "Solution Chemistry of Advanced Materials and Technologies", ITMO University, 191002 Saint Petersburg, Russia;* orcid.org/0000-0002-5081-4876; Email: vinogradov@scamt-itmo.ru

Authors

Polina I. Baburova − *International Institute "Solution Chemistry of Advanced Materials and Technologies", ITMO University, 191002 Saint Petersburg, Russia*

Daniil V. Kladko − *International Institute "Solution Chemistry of Advanced Materials and Technologies", ITMO University, 191002 Saint Petersburg, Russia*

https://doi.org/10.1021/acsnano.2c10127
ACS Nano 2023, 17, 20925−20938

Alina Lokteva − *International Institute "Solution Chemistry of Advanced Materials and Technologies", ITMO University, 191002 Saint Petersburg, Russia*
Anna Pozhitkova − *International Institute "Solution Chemistry of Advanced Materials and Technologies", ITMO University, 191002 Saint Petersburg, Russia*
Viktoriya Rumyantceva − *International Institute "Solution Chemistry of Advanced Materials and Technologies", ITMO University, 191002 Saint Petersburg, Russia*
Valeriya Rumyantceva − *International Institute "Solution Chemistry of Advanced Materials and Technologies", ITMO University, 191002 Saint Petersburg, Russia*
Ilya V. Pankov − *Institute of Physical and Organic Chemistry, Southern Federal University, 344090 Rostov-on-Don, Russia;* orcid.org/0000-0001-5302-4792
Sergey Taskaev − *National Research South Ural State University, Chelyabinsk 454080, Russia; Chelyabinsk State University, Chelyabinsk 454001, Russia*

Complete contact information is available at: https://pubs.acs.org/10.1021/acsnano.2c10127

Author Contributions

P.I.B. and D.V.K. contributed equally.

Funding

The work was financially supported by the Russian Science Foundation no. 21-73-10150. The authors also thank Priority 2030 Federal Academic Leadership Program for infrastructure support.

Notes

The authors declare no competing financial interest.

ACKNOWLEDGMENTS

The authors are grateful to the Shared Use Center "High-Resolution Transmission Electron Microscopy" (SFedU) for conducting the TEM studies.

REFERENCES

(1) Tenke, P.; Mezei, T.; Bőde, I.; Köves, B. Catheter-Associated Urinary Tract Infections. *Eur. Urol. Suppl.* **2017**, *16* (4), 138−143.
(2) Haque, M.; Sartelli, M.; McKimm, J.; Abu Bakar, M. B. Health Care-Associated Infections: an Overview. *Infect. Drug Resist.* **2018**, *11*, 2321−2333.
(3) Percival, S. L.; Suleman, L.; Vuotto, C.; Donelli, G. Healthcare-Associated Infections, Medical Devices and Biofilms: Risk, Tolerance and Control. *J. Med. Microbiol.* **2015**, *64* (4), 323−334.
(4) Ricardo, S. I. C.; Anjos, I. I. L.; Monge, N.; Faustino, C. M. C.; Ribeiro, I. A. C. A Glance at Antimicrobial Strategies to Prevent Catheter-Associated Medical Infections. *ACS Infect. Dis.* **2020**, *6* (12), 3109−3130.
(5) Infection Prevention and Control UHL. *Report on the Burden of Endemic Health Care-Associated Infection Worldwide*; World Health Organization, 2011.
(6) Stewart, S.; et al. Epidemiology of Healthcare-Associated Infection Reported from a Hospital-Wide Incidence Study: Considerations for Infection Prevention and Control Planning. *J. Hosp. Infect.* **2021**, *114*, 10−22.
(7) Gould, C. V. UC; Agarwal, R. K.; Kuntz, G.; P, D. A. Guideline for Prevention of Catheter-Associated Urinary Tract Infections. *Infect Control Hosp Epidemiol.* **2010**, *31* (4), 319−326.
(8) Neoh, K. G.; Li, M.; Kang, E.-T.; Chiong, E.; Tambyah, P. A. Surface Modification Strategies for Combating Catheter-Related Complications: Recent Advances and Challenges. *J. Mater. Chem. B* **2017**, *5* (11), 2045−2067.
(9) Nicolle, L. E. Catheter Associated Urinary Tract Infections. *Antimicrob. Resist. Infect. Control* **2014**, *3* (1), No. 23.
(10) Faustino, C. M. C.; Lemos, S. M. C.; Monge, N.; Ribeiro, I. A. C. A Scope at Antifouling Strategies to Prevent Catheter-Associated Infections. *Adv. Colloid Interface Sci.* **2020**, *284*, No. 102230.
(11) Hadjesfandiari, N.; Yu, K.; Mei, Y.; Kizhakkedathu, J. N. Polymer Brush-Based Approaches for the Development of Infection-Resistant Surfaces. *J. Mater. Chem. B* **2014**, *2* (31), 4968.
(12) Yu, K.; Alzahrani, A.; Khoddami, S.; Ferreira, D.; Scotland, K. B.; Cheng, J. T. J.; Yazdani-Ahmadabadi, H.; Mei, Y.; Gill, A.; Takeuchi, L. E.; Yeung, E.; Grecov, D.; Hancock, R. E. W.; Chew, B. H.; Lange, D.; Kizhakkedathu, J. N. Self-Limiting Mussel Inspired Thin Antifouling Coating with Broad-Spectrum Resistance to Biofilm Formation to Prevent Catheter-Associated Infection in Mouse and Porcine Models. *Adv. Healthc. Mater.* **2021**, *10* (6), No. 2001573.
(13) Mitra, D.; Kang, E.-T.; Neoh, K. G. Polymer-Based Coatings with Integrated Antifouling and Bactericidal Properties for Targeted Biomedical Applications. *ACS Appl. Polym. Mater.* **2021**, *3* (5), 2233−2263.
(14) Li, K.; Chen, J.; Xue, Y.; Ding, T.; Zhu, S.; Mao, M.; Zhang, L.; Han, Y. Polymer Brush Grafted Antimicrobial Peptide on Hydroxyapatite Nanorods for Highly Effective Antibacterial Performance. *Chem. Eng. J.* **2021**, *423*, No. 130133.
(15) Jiao, Y.; Niu, L.; Ma, S.; Li, J.; Tay, F. R.; Chen, J. Quaternary Ammonium-Based Biomedical Materials: State-of-the-Art, Toxicological Aspects and Antimicrobial Resistance. *Prog. Polym. Sci.* **2017**, *71*, 53−90.
(16) Siddiq, D. M.; Darouiche, R. O. New Strategies to Prevent Catheter-Associated Urinary Tract Infections. *Nat. Rev. Urol.* **2012**, *9* (6), 305−314.
(17) Francolini, I.; Donelli, G.; Vuotto, C.; Baroncini, F. A.; Stoodley, P.; Taresco, V.; Martinelli, A.; D'Ilario, L.; Piozzi, A. Antifouling Polyurethanes to Fight Device-Related Staphylococcal Infections: Synthesis, Characterization, and Antibiofilm Efficacy. *Pathog. Dis.* **2014**, *70* (3), 401−407.
(18) Francolini, I.; Silvestro, I.; Di Lisio, V.; Martinelli, A.; Piozzi, A. Synthesis, Characterization, and Bacterial Fouling-Resistance Properties of Polyethylene Glycol-Grafted Polyurethane Elastomers. *Int. J. Mol. Sci.* **2019**, *20* (4), 1001.
(19) Xing, C.-M.; Meng, F.-N.; Quan, M.; Ding, K.; Dang, Y.; Gong, Y.-K. Quantitative Fabrication, Performance Optimization and Comparison of PEG and Zwitterionic Polymer Antifouling Coatings. *Acta Biomater.* **2017**, *59*, 129−138.
(20) Herrwerth, S.; Eck, W.; Reinhardt, S.; Grunze, M. Factors That Determine the Protein Resistance of Oligoether Self-Assembled Monolayers − Internal Hydrophilicity, Terminal Hydrophilicity, and Lateral Packing Density. *J. Am. Chem. Soc.* **2003**, *125* (31), 9359−9366.
(21) Kowalczuk, D.; Ginalska, G.; Piersiak, T.; Miazga-Karska, M. Prevention of Biofilm Formation on Urinary Catheters: Comparison of the Sparfloxacin-Treated Long-Term Antimicrobial Catheters with Silver-Coated Ones. *J. Biomed. Mater. Res. Part B Appl. Biomater.* **2012**, *100B* (7), 1874−1882.
(22) Prateeksha, P.; Bajpai, R.; Rao, C. V.; Upreti, D. K.; Barik, S. K.; Singh, B. N. Chrysophanol-Functionalized Silver Nanoparticles for Anti-Adhesive and Anti-Biofouling Coatings to Prevent Urinary Catheter-Associated Infections. *ACS Appl. Nano Mater.* **2021**, *4* (2), 1512−1528.
(23) Phuengkham, H.; Nasongkla, N. Development of Antibacterial Coating on Silicone Surface via Chlorhexidine-Loaded Nanospheres. *J. Mater. Sci. Mater. Med.* **2015**, *26* (2), No. 78.
(24) Shalom, Y.; Perelshtein, I.; Perkas, N.; Gedanken, A.; Banin, E. Catheters Coated with Zn-Doped CuO Nanoparticles Delay the Onset of Catheter-Associated Urinary Tract Infections. *Nano Res.* **2017**, *10* (2), 520−533.
(25) Costoya, A.; Velázquez Becerra, L. E.; Meléndez-Ortiz, H. I.; Díaz-Gómez, L.; Mayer, C.; Otero, A.; Concheiro, A.; Bucio, E.; Alvarez-Lorenzo, C. Immobilization of Antimicrobial and Anti-Quorum Sensing Enzymes onto GMA-Grafted Poly(Vinyl Chloride) Catheters. *Int. J. Pharm.* **2019**, *558*, 72−81.

(26) Koo, H.; Allan, R. N.; Howlin, R. P.; Stoodley, P.; Hall-Stoodley, L. Targeting Microbial Biofilms: Current and Prospective Therapeutic Strategies. *Nat. Rev. Microbiol.* **2017**, *15* (12), 740−755.
(27) Singha, P.; Locklin, J.; Handa, H. A Review of the Recent Advances in Antimicrobial Coatings for Urinary Catheters. *Acta Biomater.* **2017**, *50*, 20−40.
(28) Krzyżek, P. Challenges and Limitations of Anti-Quorum Sensing Therapies. *Front. Microbiol.* **2019**, *10*, DOI: 10.3389/fmicb.2019.02473.
(29) Valiei, A.; Lin, N.; Bryche, J.-F.; McKay, G.; Canva, M.; Charette, P. G.; Nguyen, D.; Moraes, C.; Tufenkji, N. Hydrophilic Mechano-Bactericidal Nanopillars Require External Forces to Rapidly Kill Bacteria. *Nano Lett.* **2020**, *20* (8), 5720−5727.
(30) Zhao, S.; Li, Z.; Linklater, D. P.; Han, L.; Jin, P.; Wen, L.; Chen, C.; Xing, D.; Ren, N.; Sun, K.; Juodkazis, S.; Ivanova, E. P.; Jiang, L. Programmed Death of Injured Pseudomonas Aeruginosa on Mechano-Bactericidal Surfaces. *Nano Lett.* **2022**, *22*, 1129.
(31) Protasiuk, L. E.; Serov, N. S.; Lokteva, A. V.; Kladko, D. V.; Koshel, E. I.; Vinogradov, V. V. Mechano-Bactericidal Anisotropic Particles for Oral Biofilm Treatment. *J. Mater. Chem. B* **2022**, *10* (25), 4867−4877.
(32) Wang, L.; Meng, Z.; Chen, Y.; Zheng, Y. Engineering Magnetic Micro/Nanorobots for Versatile Biomedical Applications. *Adv. Intell. Syst.* **2021**, *3* (7), No. 2000267.
(33) Wang, X.; Law, J.; Luo, M.; Gong, Z.; Yu, J.; Tang, W.; Zhang, Z.; Mei, X.; Huang, Z.; You, L.; Sun, Y. Magnetic Measurement and Stimulation of Cellular and Intracellular Structures. *ACS Nano* **2020**, *14*, 3805.
(34) Zhou, H.; Mayorga-Martinez, C. C.; Pané, S.; Zhang, L.; Pumera, M. Magnetically Driven Micro and Nanorobots. *Chem. Rev.* **2021**, *121*, 4999.
(35) Kim, Y.; Parada, G. A.; Liu, S.; Zhao, X. Ferromagnetic Soft Continuum Robots. *Sci. Robot.* **2019**, *4* (33), DOI: 10.1126/scirobotics.aax7329.
(36) Dong, Y.; Wang, L.; Xia, N.; Yang, Z.; Zhang, C.; Pan, C.; Jin, D.; Zhang, J.; Majidi, C.; Zhang, L. Untethered Small-Scale Magnetic Soft Robot with Programmable Magnetization and Integrated Multifunctional Modules. *Sci. Adv.* **2022**, *8* (25), DOI: 10.1126/sciadv.abn8932.
(37) Wu, Y.; Zhang, S.; Yang, Y.; Li, Z.; Wei, Y.; Ji, Y. Locally Controllable Magnetic Soft Actuators with Reprogrammable Contraction-Derived Motions. *Sci. Adv.* **2022**, *8* (25), DOI: 10.1126/sciadv.abo6021.
(38) Rosenfeld, D.; Field, H.; Kim, Y. J.; Pang, K. K. L.; Nagao, K.; Koehler, F.; Anikeeva, P. Magnetothermal Modulation of Calcium-Dependent Nerve Growth. *Adv. Funct. Mater.* **2022**, *32*, 0224558.
(39) Hescham, S.-A.; Chiang, P.-H.; Gregurec, D.; Moon, J.; Christiansen, M. G.; Jahanshahi, A.; Liu, H.; Rosenfeld, D.; Pralle, A.; Anikeeva, P.; Temel, Y. Magnetothermal Nanoparticle Technology Alleviates Parkinsonian-like Symptoms in Mice. *Nat. Commun.* **2021**, *12* (1), No. 5569.
(40) Zakharzhevskii, M. A.; Anastasova, E. I.; Kladko, D. V.; Prilepskii, A. Y.; Gorshkova, M. N.; Vinnik, D. A.; Taskaev, S. V.; Vinogradov, V. V. Shape Anisotropic Magnetic Thrombolytic Actuators: Synthesis and Systematic Behavior Study. *J. Mater. Chem. B* **2021**, *9* (24), 4941−4955.
(41) Dong, Y.; Wang, L.; Yuan, K.; Ji, F.; Gao, J.; Zhang, Z.; Du, X.; Tian, Y.; Wang, Q.; Zhang, L. Magnetic Microswarm Composed of Porous Nanocatalysts for Targeted Elimination of Biofilm Occlusion. *ACS Nano* **2021**, *15*, 5056.
(42) Hwang, G.; Paula, A. J.; Hunter, E. E.; Liu, Y.; Babeer, A.; Karabucak, B.; Stebe, K.; Kumar, V.; Steager, E.; Koo, H. Catalytic Antimicrobial Robots for Biofilm Eradication. *Sci. Robot.* **2019**, *4* (29), DOI: 10.1126/scirobotics.aaw2388.
(43) Sun, M.; Chan, K. F.; Zhang, Z.; Wang, L.; Wang, Q.; Yang, S.; Chan, S. M.; Chiu, P. W. Y.; Sung, J. J. Y.; Zhang, L. Magnetic Microswarm and Fluoroscopy-Guided Platform for Biofilm Eradication in Biliary Stents. *Adv. Mater.* **2022**, *34* (34), No. 2201888.
(44) Kim, Y.; Zhao, X. Magnetic Soft Materials and Robots. *Chem. Rev.* **2022**, *122* (5), 5317−5364.
(45) Pozhitkova, A. V.; Kladko, D. V.; Vinnik, D. A.; Taskaev, S. V.; Vinogradov, V. V. Reprogrammable Soft Swimmers for Minimally Invasive Thrombus Extraction. *ACS Appl. Mater. Interfaces* **2022**, *14* (20), 23896−23908.
(46) Kim, Y.; Genevriere, E.; Harker, P.; Choe, J.; Balicki, M.; Regenhardt, R. W.; Vranic, J. E.; Dmytriw, A. A.; Patel, A. B.; Zhao, X. Telerobotic Neurovascular Interventions with Magnetic Manipulation. *Sci. Robot.* **2022**, *7* (65), DOI: 10.1126/scirobotics.abg9907.
(47) Xu, T.; Zhang, J.; Salehizadeh, M.; Onaizah, O.; Diller, E. Millimeter-Scale Flexible Robots with Programmable Three-Dimensional Magnetization and Motions. *Sci. Robot.* **2019**, *4* (29), DOI: 10.1126/scirobotics.aav4494.
(48) Wu, Y.; Dong, X.; Kim, J.; Wang, C.; Sitti, M. Wireless Soft Millirobots for Climbing Three-Dimensional Surfaces in Confined Spaces. *Sci. Adv.* **2022**, *8* (21), DOI: 10.1126/sciadv.abn3431.
(49) Wang, T.; Ugurlu, H.; Yan, Y.; Li, M.; Li, M.; Wild, A. M.; Yildiz, E.; Schneider, M.; Sheehan, D.; Hu, W.; Sitti, M. Adaptive Wireless Millirobotic Locomotion into Distal Vasculature. *Nat. Commun.* **2022**, *13* (1), DOI: 10.1038/s41467-022-32059-9.
(50) COMPACT CATH. Urinary Catheter Types and Sizes and How to Choose https://www.compactcath.com/blog/catheter-types-and-sizes/ (accessed 2023−10−14).
(51) Liao, Z.; Hossain, M.; Yao, X.; Navaratne, R.; Chagnon, G. A Comprehensive Thermo-Viscoelastic Experimental Investigation of Ecoflex Polymer. *Polym. Test.* **2020**, *86*, No. 106478.
(52) Mohapatra, J.; Xing, M.; Elkins, J.; Beatty, J.; Liu, J. P. Extraordinary Magnetic Hardening in Nanowire Assemblies: The Geometry and Proximity Effects. *Adv. Funct. Mater.* **2021**, *31* (13), No. 2010157.
(53) Gandha, K.; Mohapatra, J.; Liu, J. P. Coherent Magnetization Reversal and High Magnetic Coercivity in Co Nanowire Assemblies. *J. Magn. Magn. Mater.* **2017**, *438*, 41−45.
(54) Xie, B.; Qian, Y.; Zhang, S.; Fu, S.; Yu, W. A Hydrothermal Reduction Route to Single-Crystalline Hexagonal Cobalt Nanowires. *Eur. J. Inorg. Chem.* **2006**, *2006* (12), 2454−2459.
(55) Parkes, L. M.; Hodgson, R.; Lu, L. T.; Tung, L. D.; Robinson, I.; Fernig, D. G.; Thanh, N. T. K. Cobalt Nanoparticles as a Novel Magnetic Resonance Contrast Agent-Relaxivities at 1.5 and 3 T. *Contrast Media Mol. Imaging* **2008**, *3* (4), 150−156.
(56) Heinrich, G.; Klüppel, M.; Vilgis, T. A. Reinforcement of Elastomers. *Curr. Opin. Solid State Mater. Sci.* **2002**, *6* (3), 195−203.
(57) Kim, B.; Kim, D.-H.; Jung, J.; Park, J.-O. A Biomimetic Undulatory Tadpole Robot Using Ionic Polymer−Metal Composite Actuators. *Smart Mater. Struct.* **2005**, *14* (6), 1579−1585.
(58) Wang, X.; Mao, G.; Ge, J.; Drack, M.; Santiago, G.; Bermúdez, C.; Wirthl, D.; Illing, R.; Kosub, T.; Bischoff, L.; Wang, C.; Fassbender, J.; Kaltenbrunner, M.; Makarov, D. Untethered and Ultrafast Soft-Bodied Robots. *Commun. Mater.* **2020**, DOI: 10.1038/s43246-020-00067-1.
(59) Wang, Z.; Hang, G.; Li, J.; Wang, Y.; Xiao, K. A Micro-Robot Fish with Embedded SMA Wire Actuated Flexible Biomimetic Fin. *Sensors Actuators A Phys.* **2008**, *144* (2), 354−360.
(60) Zhao, Q.; Liu, S.; Chen, J.; He, G.; Di, J.; Zhao, L.; Su, T.; Zhang, M.; Hou, Z. Fast-Moving Piezoelectric Micro-Robotic Fish with Double Caudal Fins. *Rob. Auton. Syst.* **2021**, *140*, No. 103733.
(61) Elgeti, J.; Winkler, R. G.; Gompper, G. Physics of Microswimmers - Single Particle Motion and Collective Behavior: A Review. *Rep. Prog. Phys.* **2015**, *78* (5), 056601.
(62) Li, D.; Jeong, M.; Oren, E.; Yu, T.; Qiu, T. A Helical Microrobot with an Optimized Propeller-Shape for Propulsion in Viscoelastic Biological Media. *Robotics* **2019**, *8* (4), 87.
(63) Li, M.; Matouš, K.; Nerenberg, R. Predicting Biofilm Deformation with a Viscoelastic Phase-field Model: Modeling and Experimental Studies. *Biotechnol. Bioeng.* **2020**, *117* (11), 3486−3498.
(64) Tierra, G.; Pavissich, J. P.; Nerenberg, R.; Xu, Z.; Alber, M. S. Multicomponent Model of Deformation and Detachment of a Biofilm under Fluid Flow. *J. R. Soc. Interface* **2015**, *12* (106), No. 20150045.
(65) Zhao, J.; Shen, Y.; Haapasalo, M.; Wang, Z.; Wang, Q. A 3D Numerical Study of Antimicrobial Persistence in Heterogeneous Multi-Species Biofilms. *J. Theor. Biol.* **2016**, *392*, 83−98.

(66) Dreszer, C.; Wexler, A. D.; Drusová, S.; Overdijk, T.; Zwijnenburg, A.; Flemming, H.-C.; Kruithof, J. C.; Vrouwenvelder, J. S. In-Situ Biofilm Characterization in Membrane Systems Using Optical Coherence Tomography: Formation, Structure, Detachment and Impact of Flux Change. *Water Res.* **2014**, *67*, 243−254.
(67) Kladko, D. V.; Vinogradov, V. V. Magnetosurgery: Principles, Design, and Applications. *Smart Mater. Med.* **2024**, *5*, 24−35.
(68) Yang, Z.; Zhang, L. Magnetic Actuation Systems for Miniature Robots: A Review. *Adv. Intell. Syst.* **2020**, *2* (9), No. 2000082.
(69) Dong, Y.; Wang, L.; Zhang, Z.; Ji, F.; Chan, T. K. F.; Yang, H.; Chan, C. P. L.; Yang, Z.; Chen, Z.; Chang, W. T.; Chan, J. Y. K.; Sung, J. J. Y.; Zhang, L. Endoscope-Assisted Magnetic Helical Micromachine Delivery for Biofilm Eradication in Tympanostomy Tube. *Sci. Adv.* **2022**, *8* (40), DOI: 10.1126/sciadv.abq8573.
(70) Gloag, E. S.; Fabbri, S.; Wozniak, D. J.; Stoodley, P. Biofilm Mechanics: Implications in Infection and Survival. *Biofilm* **2020**, *2*, No. 100017.
(71) Fabbri, S.; Johnston, D. A.; Rmaile, A.; Gottenbos, B.; De Jager, M.; Aspiras, M.; Starke, E. M.; Ward, M. T.; Stoodley, P. Streptococcus Mutans Biofilm Transient Viscoelastic Fluid Behaviour during High-Velocity Microsprays. *J. Mech. Behav. Biomed. Mater.* **2016**, *59*, 197−206.
(72) Fabbri, S.; Li, J.; Howlin, R. P.; Rmaile, A.; Gottenbos, B.; De Jager, M.; Starke, E. M.; Aspiras, M.; Ward, M. T.; Cogan, N. G.; Stoodley, P. Fluid-Driven Interfacial Instabilities and Turbulence in Bacterial Biofilms. *Environ. Microbiol.* **2017**, *19* (11), 4417−4431.
(73) Gandha, K.; Elkins, K.; Poudyal, N.; Liu, X.; Liu, J. P. High Energy Product Developed from Cobalt Nanowires. *Sci. Rep.* **2014**, *4* (1), No. 5345.

https://doi.org/10.1021/acsnano.2c10127
ACS Nano 2023, 17, 20925−20938